Zwitterion functionalized gold nanoclusters for multimodal near infrared fluorescence and photoacoustic imaging

Danjin Shen, Maxime Henry, Vanessa Trouillet, Clothilde Comby-Zerbino, Franck Bertorelle, Lucie Sancey, Rodolphe Antoine, Jean-Luc Coll, Véronique Josserand, and Xavier Le Guével

Citation: APL Materials **5**, 053404 (2017); doi: 10.1063/1.4977203
View online: https://doi.org/10.1063/1.4977203
View Table of Contents: http://aip.scitation.org/toc/apm/5/5
Published by the American Institute of Physics

Zwitterion functionalized gold nanoclusters for multimodal near infrared fluorescence and photoacoustic imaging

Danjin Shen,[1] Maxime Henry,[1] Vanessa Trouillet,[2] Clothilde Comby-Zerbino,[3] Franck Bertorelle,[3] Lucie Sancey,[1] Rodolphe Antoine,[3] Jean-Luc Coll,[1] Véronique Josserand,[1] and Xavier Le Guével[1,a]

[1]*Cancer Targets and Experimental Therapeutics, Institute for Advanced Biosciences (IAB), INSERM-U1209/CNRS-UMR 5309, University of Grenoble Alpes (UGA), 38000 Grenoble, France*

[2]*Institute for Applied Materials (IAM) and Karlsruhe Nano Micro Facility (KNMF), Karlsruhe Institute of Technology (KIT), Eggenstein-Leopoldshafen, Germany*

[3]*Institut Lumière Matière, UMR 5306, Université Claude Bernard Lyon 1-CNRS, Université de Lyon, 69622 Villeurbanne Cedex, France*

(Received 12 December 2016; accepted 26 January 2017; published online 1 March 2017)

Gold nanoclusters (Au NCs) are an emerging type of theranostic agents combining therapeutic and imaging features with reduced toxicity. Au NCs stabilized by a zwitterion ligand with a fine control of the metal core size and the ligand coverage were synthesized by wet chemistry. Intense fluorescence signal is reported for the highest ligand coverage, whereas photoacoustic signal is stronger for the largest metal core. The best Au NC candidate with an average molecular weight of 17 kDa could be detected with high sensitivity on a 2D-near-infrared imaging instrument (limit of detection (LOD) = 2.3 μM) and by photoacoustic imaging. *In vitro* and *in vivo* experiments demonstrate an efficient cell uptake in U87 cell lines, a fast renal clearance ($t_{1/2\alpha}$ = 6.5 ± 1.3 min), and a good correlation between near infrared fluorescence and photoacoustic measurements to follow the early uptake of Au NCs in liver. [http://dx.doi.org/10.1063/1.4977203]

The sub-class of nanoclusters (NCs) in a wide library of metal nanoparticles has found a growing interest over the last few years for *in vivo* studies notably for cancer applications. Those metal NCs, mainly gold, are made of ten to hundred atoms and usually presented as species filling the gap between molecules and nanoparticles.[1–4] Gold nanoclusters (Au NCs) present several features making them appealing for cancer therapy thanks to (i) their high renal clearance[5,6] reducing toxicity risk, (ii) the relatively high tumor retention by passive uptake,[7,8] (iii) the ability to trigger cell death under light illumination[9] or radiosensitization,[10–12] and (iv) the detection by multimodal imaging techniques.[13–15]

In optical imaging, one of the great advantages of Au NCs compared to plasmonic Au nanoparticles (Au NPs) is related to the ability to visualize them by fluorescence in the red-near-infrared (NIR) region (650-800 nm), a spectral window suitable for *in vivo* studies due to the reduced tissue scattering and low blood absorption.[16,17] In addition, the high electronic number of gold (Z = 79) allows the detection of gold particles by computed X-ray tomography (CT)[5] and by photoacoustic imaging (PAI).[18,19] With the development of new contrast agents such as gold nanorods and nanocages, PAI combines the most compelling features of optical imaging and ultrasound imaging, providing both high optical contrast and high resolution ultrasound including *in vivo* in deep tissues.[20–22]

Au NCs stabilized by glutathione (GSH) are probably one of the most described NCs in the literature with a precise control of their size and their structure.[23–26] The natural peptide GSH has a zwitterionic structure and, when coated on the particle surface, could prevent the detection by

[a]Author to whom correspondence should be addressed. Electronic mail: xavier.le-guevel@univ-grenoble-alpes.fr

macrophages.[27] Recently, we investigated the optical properties and the behavior in cell environment of Au NCs stabilized by bidentate thiol zwitterionic ligand (Zw) have been recently reported showing a high colloidal stability and an intense fluorescence emission tunable in the near-infrared region .[28–30]

In this study, we aimed to determine the influence of the core size and the ligand coverage of gold particle to their fluorescence and their photoacoustic signals. For this purpose, gold particles of different sizes from the small plasmonic NPs (i.e., size ∼4 nm) to NCs (i.e., size < 2.5 nm) stabilized by a zwitterion ligand were prepared. Then, we investigated the behavior of the best candidate exhibiting both high fluorescence and photoacoustic signals in cells and in mice. Additional information is also reported on the NC size determined by mass spectrometry for Au NCs stabilized by a zwitterionic ligand.

All products were purchased from Sigma Aldrich and MilliQ (Millipore, France) water was used for all experiments.

Thioctic-zwitterion (Zw, $C_{15}H_{30}N_2O_4S_3$, M∼399 g mol^{-1}) was synthesized following the protocol described elsewhere.[28] Au NCs with zwitterion (Au:Zw) were prepared by the addition of gold salt ($HAuCl_4.3H_2O$, 50 mM) to a basic solution (pH 10) containing the ligand in the presence of the strong reducing agent $NaBH_4$ (50 mM) and stirred for 15 h. Zwitterion stabilized Au NCs were synthesized with the molar ratio Au:Zw:$NaBH_4$ = 1:1:2, 1:2:2, and 1:5:2. Zwitterion stabilized Au NPs were synthesized with the molar ratio Au:Zw:$NaBH_4$ = 2:1:2 and 5:1:2. Afterwards, solutions were filtered twice with Amicon 3 kDa cut-off filters at 13 600 rpm for 20 min to remove excess free ligands, adjusted to pH 7, concentrated to 5 mg gold/ml in water, and kept refrigerated until use.

Protected $Au_{25}GSH_{18}$ clusters were synthesized in two steps as described by Pradeep and coworkers.[31] Briefly, in a first step, the complex formed between $HAuCl_4$ and glutathione GSH (Au:GSH = 1:4) was reduced in a methanolic solution (0 °C) with $NaBH_4$. The resulting precipitate (Au@SG) was washed with methanol and dried. In a second step, Au@SG was dissolved in water with 1 mM of GSH and heated at 55 °C for 12 h. The solution was centrifuged and $Au_{25}GSH_{18}$ is precipitated from the supernatant by adding methanol. The precipitate was washed several times with methanol before drying in vacuum.

Transmission electron microscopy (TEM) images of the NCs and NPs were measured on a FEI Tecnai G2 Twin TEM. XPS investigation was performed in a K-Alpha+ spectrometer (ThermoFisher Scientific) using a microfocused, monochromated Al Kα X-ray source (400 μM spot size). The spectra were fitted with one or more Voigt profiles (binding energy uncertainty: ±0.2 eV) and Scofield sensitivity factors were applied for quantification.[32] All spectra were referenced to the C1s peak at 285.0 eV binding energy (C–C, C–H) and controlled by means of the well-known photoelectron peaks of Cu, Ag, and Au, respectively. Measurements were performed at two different locations of dried samples. Evolution of the Au NC size as a function of the metal–ligand ratio was determined by electrospray ionization (ESI) on a commercial quadrupole time-of-flight (micro-qTOF, Bruker-Daltonics, Bremen, Germany, mass resolution ∼10 000). The samples were prepared by diluting the mother solution in water, to a final concentration of 0.25-0.5 mg ml^{-1} in 50/50% water/meOH v/v. The samples were analyzed in positive ion mode: each data point was the summation of spectra over 5 min. External calibration was carried out with a set of synthetic peptides.

Absorbance measurements on diluted samples were performed on an Evolution 201 (Thermoscientific) UV-vis spectrophotometer between 300 and 1000 nm. Fluorescence spectra were recorded on a Perkin Elmer LS45 fluorescence spectrometer. Fluorescence imaging was performed with a NIR 2D-fluorescence reflectance imaging device (Fluobeam 800®, Fluoptics, France). The excitation is provided by a class 1 expanded laser source at 780 nm, and the irradiance on the imaging field is 100 mW/cm^2. The fluorescence signal is collected by a CCD through a high pass filter with a high transmittance for wavelength >830 nm.

PAI was performed on The VevoLAZR system (Visualsonics, Fujifilm) using the LZ201 transducer (256 elements linear array; 9-18 MHz) allowing a 44 μM axial resolution. The laser is tunable between 680 and 970 nm, and acquisitions can be made continuously with 1 nm steps providing a photoacoustic spectrum.

U87MG cells were cultured in six-well plates one day before the experiment. The Au NCs were added to the cell medium at 50 μg gold/ml (eq. 35 μM) for the indicated time (4 h to 24 h), and the

cells were incubated at 37 °C or 4 °C. Then, the cells were resuspended with trypsin and carefully washed in phosphate-buffered saline (PBS) before analysis. Propidium iodide was added to the cell suspension according to the manufacturer's instructions (BD Pharmingen, Belgium). The cells were analyzed using LSR II (Becton Dickinson, France). The 405 nm laser was used to excite the Au NCs, and the signal was collected after a long-pass 750 nm, at 780/60 nm. Propidium iodide was excited at 488 nm, filtered with the long-pass 655 nm, and its emission was collected at 660/20 nm. Specific compensations were applied to prevent the overlapping of the signals.

Six weeks old NMRI nude mice (Janvier, France) were anesthetized (air/isoflurane 4% for induction and 1.5% thereafter) and were injected intravenously via the tail vein with 200 μL of Au NCs at 600 μM. *In vivo* fluorescence imaging was performed before and 1, 3, 5, and 24 h after injection. Mice were euthanized at 1, 5, or 24 h post injection (n = 3 mice per time point) and organs were harvested for *ex vivo* fluorescence imaging.

Three other mice were injected and blood samples were collected 10 s and 5, 10, 15, 20, 30, 45, and 60 min after injection and were centrifuged (10 min at 2000 g) to separate plasma. Fluorescence imaging was then performed on plasma samples.

For PAI, an US gel (Parker Laboratories, Inc., USA) was applied on the mouse body, the transducer was placed above the liver, and a 30×30 mm^2 slice was imaged both in B-mode (ultrasound) and in PA mode at 710 nm before and 1, 5, and 24 h after intravenous injection.

We choose the ligand Zw (Figure 1(a)) to produce gold particles of different sizes because this molecule was shown to strongly improve the colloidal stability of particle[33] and also to obtain Au NCs exhibiting one the highest fluorescence intensity reported so far.[28,30,34] Molar ratio Au:ligand has been modified during the synthesis in order to play both on the final metal core size and on the ligand coverage. Thus, a molar ratio Au > ligand leads to NP for Au:Zw = 2:1 and 5:1 and a molar ratio Au ≤ ligand leads to NCs for Au:Zw = 1:1, 1:2, and 1:5. TEM images (Figure S1 of the supplementary material) show clearly a decrease of the metal core diameter when the amount of the ligand increases from 4.8 ± 1.2 nm for Au:Zw 5:1 to less than 2.5 nm for Au:Zw 1:2 and Au:Zw 1:5. In the case of Au NCs (i.e., for Au:Zw 1:1, Au:Zw 1:2, and Au:Zw 1:5), mass spectrometry is reckoned as a suited technique to determine the full size and the structure of metal NCs.[35–40] We previously attempted to determine specific magic clusters using matrix-assisted laser desorption ionization / time of flight (MALDI-Tof) technique on those types of NCs without any success.[28] Here, the high mass setting is optimized for the Au:Zw NCs. Au:Zw NCs contain multiple groups capable of being ionized and the ESI source can produce highly charged ions. For those molecules that can sustain multiple charges, a distribution of charge states is often observed in the mass-to-charge spectrum. This multiplicity of states gives rise to an "envelope" of peaks in the spectrum. The distribution of charges is observed in the m/z range 1000–8000 after electrospraying in positive mode water solution containing the nanoparticles (Figure S2 of the supplementary material). Although the position of the peaks in the mass spectra is stable, the relative abundance of the different peaks is found to be slightly dependent on the electrospray mass spectrometry (ESI-MS) conditions. A multiplicative correlation algorithm (MCA) is used to estimate the mass of nanoparticles from the mass-to-charge spectra produced by electrospray ionization mass spectrometry.[41] The multiplicative correlation is designed to enhance the deconvoluted signal when the parent molecule is distributed into several charge states in the spectrum measured. This approach is summarized by the following formula:[42]

$$f(m) = \prod_{z=z_0}^{z_1} g(m/z)/g_{rms},$$

where $f(m)$ is the intensity calculated in the spectrum for mass m, $g(m/z)$ is the intensity in the mass-to charge spectrum, and g_{rms} is the root-mean-square (rms) value of the signal measured.

As the Au NCs contain multiple ionized groups (Zw ligands), a distribution of charge states is observed in the mass-to-charge spectrum, and the MCA is used to estimate the mass of the Au NCs from the mass-to-charge spectra produced by the ESI-MS. As seen in Figure 1(b), for Au:Zw 1:1, the distribution is centered at 11 000 Da with a second distribution (with a smaller intensity) at ~13 500 Da. For Au:Zw 1:2, the mass increased to 17 200 Da (with a second distribution with a smaller intensity at ~13 600 Da). For Au:Zw 1:5, the mass reached to 32 850 Da (with a second distribution at ~30 660 Da and a third at ~28 600 Da). Therefore, an obvious increase of the molecular

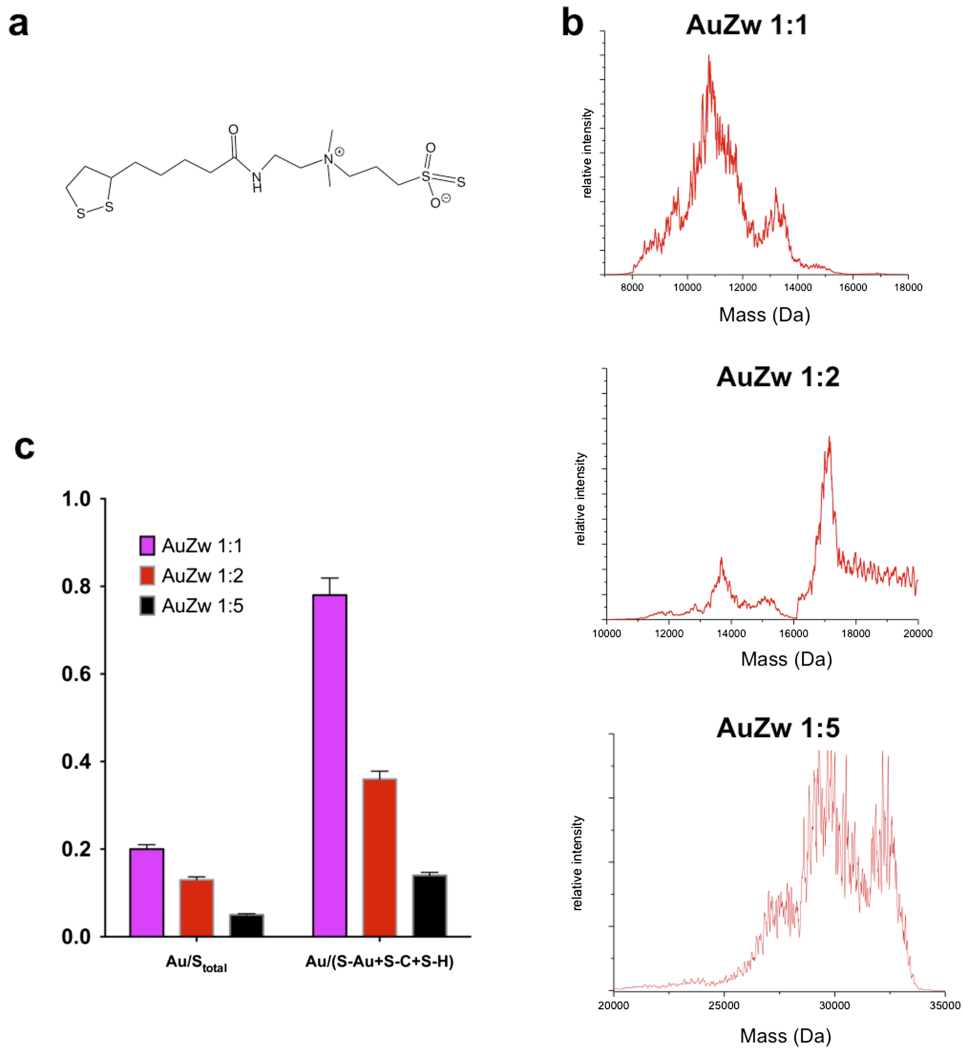

FIG. 1. (a) Chemical formula of the thioctic bidentate zwitterionic ligand Zw. (b) Deconvoluted ESI-MS spectra of Au:Zw 1:1, Au:Zw 1:2, and Au:Zw 1:5. (c) Concentration of gold (atomic%) with respect to the total concentration of sulphur (S_{total}) or to the concentration of sulphur bound to gold, carbon, and thiol (S–Au + S–C + S–H) from Zw extracted from XPS measurements.

weight of Au NCs occurs when the ligand content increases as previously reported.[28] However in this study, we obtain a higher resolution in terms of size distribution thanks to the presence of an "envelope" of peaks in the spectrum and the multiplicative correlation algorithm designed to enhance the deconvoluted signal originated from the NCs. XPS experiments provide information about the atomic concentration of each element and the nature of interaction within the sample. Contribution of gold from the core bound directly to Zw via thiol groups and compared to the total amount of the ligand could be followed by looking at the binding energy of S 2p, in particular the component at 161.8 eV characteristic for S-Au (Figure S3 of the supplementary material). In Figure 1(c), the ratio of gold concentration to the total concentration of sulphur (Au/S_{total}) or to the concentration of sulphur bound to gold, hydrogen, and carbon (Au/(S–Au + S–C + S–H)) indicates a constant decrease when Zw increases. This behavior confirms that Zw continues to bind Au core even at the molar ratio Au:Zw = 1:5. Au_nZw_m stoichiometry is then evaluated based on the average mass estimated with deconvoluted ESI mass spectra and XPS results (giving access to Au/S ratio). Results show m > n by a factor m/n higher than 2 for Au:Zw 1:1, Au:Zw 1:2, and Au:Zw 1:5, which is different, for instance, from the one reported for thiolated-protected clusters using glutathione.[4] Thus, the formation of Au:Zw

could be seen rather like an organic charged layer coated onto ultra-small gold particles. The high reactivity of the bidentate thioctic group of Zw to control Au NC growth and the strong electrostatic interaction between sulfonate and ammonium in Zw might prevent the identification of magic size "superatom".

Absorbance measurements of Au:Zw sols show the standard plasmonic band at λ = 520 nm for Au:Zw 5:1 and Au:Zw 2:1 and usually observed for Au NPs with size above 3 nm.[1] Increase of the ligand content during the synthesis leads to the fall of the plasmonic band with a decrease of the UV band absorption (Figure S4 of the supplementary material). We can see an isobectic point at λ = 420 nm between Au:Zw 1:2 and Au:Zw 1:5 that could be attributed to the absorption of the ligand Zw in the UV-visible region.[28] Fluorescence (Figure S5 of the supplementary material) is strongly enhanced when Zw > Au with a rise at λ = 820 nm followed up by a blue-shift to λ = 750 nm like it was previously reported.[28] Plasmonic NPs exhibit very weak or no fluorescence.[43] However, Au:Zw 2:1 sample still presents some fluorescence signal despite the presence of a plasmon band. This effect could be related either to the presence of smaller NCs observed in high-resolution transmission electron microscopy (HRTEM) that cannot be separated to the NPs in the solution due to the low variation in weight or to the weak quenching effect of plasmonic NP due to the small particle size.

Fluorescence intensity of the aqueous Au:Zw sols (2 mg gold/ml) prepared at different molar ratios of Au:Zw was measured on a NIR 2D-fluorescence reflectance imaging device ($\lambda_{exc.}$ 780 nm; long pass (LP) 830 nm). This medical device is dedicated to non-invasive or intraoperative *in vivo* imaging and has been used to guide surgical procedures.[44,45] Phantom imaging illustrated in Figure 2(a) shows an exponential enhancement of the fluorescence intensity when increasing Zw content with the highest signal for Au:Zw 1:5, which is in agreement with the fluorescence measurements obtained on the spectrofluorimeter. The same trend is observed with a series of dilution up to 100 µg gold/ml from the concentrated Au:Zw sols to insure no self-absorption in this concentration window.

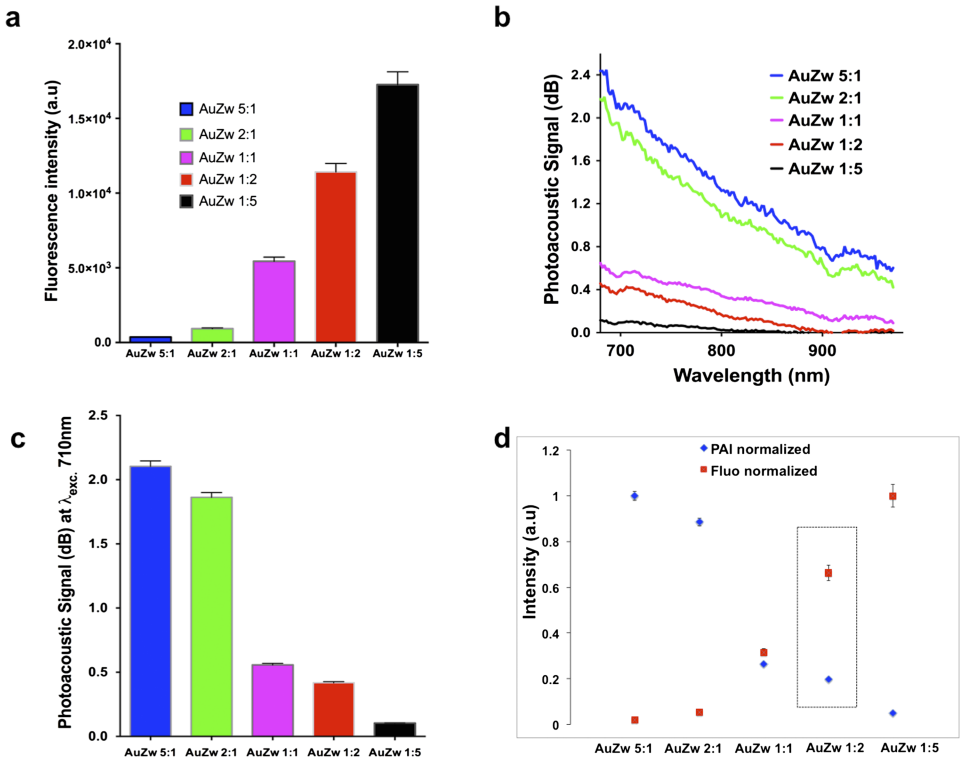

FIG. 2. (a) Fluorescence intensity of Au:Zw sols (2 mg gold/ml) measured with a NIR 2D-fluorescence reflectance imaging device ($\lambda_{exc.}$ 780 nm; LP 830 nm). Photoacoustic signal of Au:Zw sols (2 mg gold/ml) (b) between 690 and 970 nm and (c) at $\lambda_{exc.}$ 710 nm. (d) Normalized fluorescence and photoacoustic signals for Au:Zw (2 mg gold/ml).

Photoacoustic signal of the different Au:Zw sols exhibit a similar profile (Figure 2(b)) with a constant decrease of the intensity at longer wavelength from 680 nm to 910 nm followed by a slight augmentation until λ = 930 nm and then decreases again. In Figure 2(c), photoacoustic signal of Au:Zw is plotted by fixing the wavelength at λ = 710 nm and drops drastically when Zw content increased especially between Au:Zw 2:1 and Au:Zw 1:1. Evolution of normalized fluorescence and photoacoustic signals is illustrated in Figure 2(d) and shows an opposite trend with a stronger fluorescent signal for Au:Zw 1:5 whereas Au:Zw 5:1 exhibits the highest photoacoustic signal. This observation could be logically explained by the fact that high ligand coverage surrounding the metal core of the NCs improves the rigidity of the network leading to a strong fluorescence intensity.[46] Inversely, particle with a bigger metal core like for Au:Zw 2:1 and Au:Zw 5:1 with size > 4 nm will produce heat under illumination leading to more intense vibration and then stronger photoacoustic signal.

We then decided to select the sample Au:Zw 1:2 as the optimal candidate for *in vitro* and *in vivo* experiments because it exhibits both quite intense fluorescence and enough signal to be detected by PAI. Knowing the molecular weight of Au:Zw 1:2 ~17 kDa, and the weight concentration of gold per sample (~50%), Au:Zw concentration could be then expressed in M (mol/l) in this study. Fluorescence calibration of Au:Zw 1:2 between 4.5 μM and 600 μM suggests a limit of detection to 2.3 μM by fixing a signal/noise = 2 using PBS solution as control (Figure 3(a)). This sensitivity can be considered as relatively high taking account of the low absorption of Au NCs at this excitation wavelength (see absorbance and fluorescence emission Figures S4 and S5). Photoacoustic calibration in Figure 3(b) indicates a linear behaviour between 70 and 600 μM with signal >0.2 at 140 μM.

In vitro cell studies have been performed on glioblastoma cells in culture (U87MG) incubating those cells with Au:Zw 1:2 at 35 μM in complete medium during 4, 8, or 24 h. Flow cytometry analysis illustrated in Figure 4(a) indicates an enhancement of the fluorescent signal in cells originated from the Au NCs over time (quantification reported in Figure 4(c)) reaching more than 90% after 24 h of incubation. Experiment performed at 4 °C shows a very weak Au NC uptake in cells after 4 h of incubation with less than 5% positive cells compared to the same experiment set at 37 °C with 20.96% positive cells. This result confirms the low passive diffusion of those particles suggesting that Au:Zw 1:2 probably accumulates on the cell surface before an uptake by active process.[29,30,47] Cytotoxicity assays have been performed using propidium iodide (Figures 4(b) and 4(c)) and show no significant toxicity (<3%) until 24 h incubation and even using Au NC concentration up to 100 μM (data no shown).

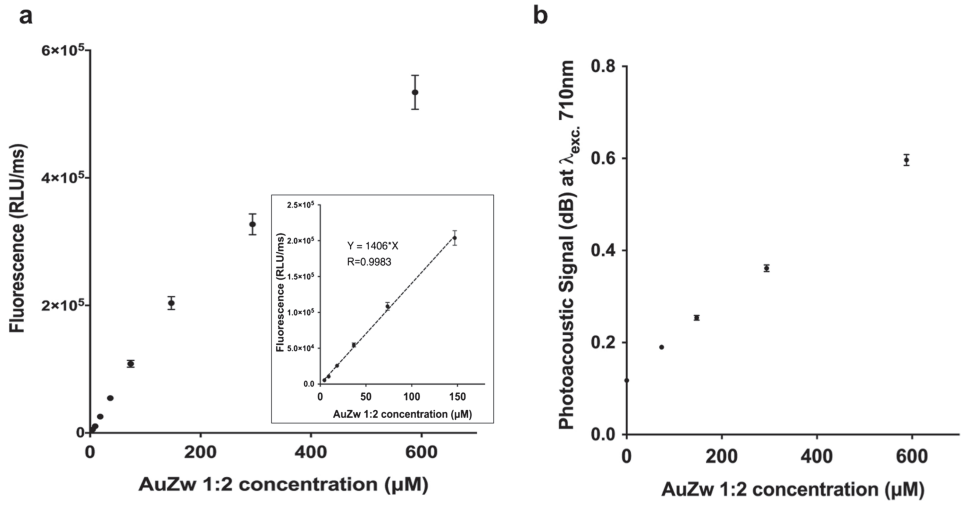

FIG. 3. (a) Calibration of Au:Zw 1:2 fluorescence intensity between 4.5 and 600 μM in water measured with a NIR 2D-fluorescence reflectance imaging device ($\lambda_{exc.}$ 780 nm; LP 830 nm). (b) Calibration of Au:Zw 1:2 photoacoustic signal between 70 and 600 μM in water.

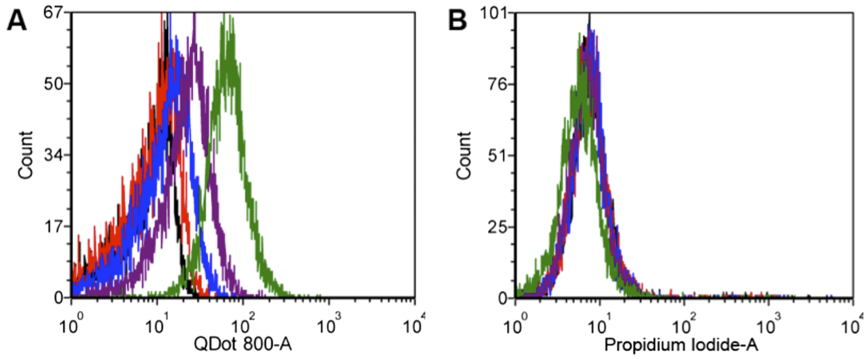

C

Condition	% of positive cells to AuNC	% of positive cells to propidium iodide
Control	1.06	1.98
4h-4°C	4.57	2.00
4h-37°C	20.96	1.63
8h	57.43	1.59
24h	97.57	1.26

FIG. 4. ((a) and (c)) Flow cytometry results and ((b) and (c)) toxicity tests by propidium iodide on U87MG cells incubated with Au:Zw 1:2 (35 μM in complete medium) at different time points and at 37 °C and at 4 °C for 4 h.

Blood pharmacokinetic of Au:Zw 1:2 (M~17 kDa; 600 μM in PBS) was measured by fluorescence imaging and shows a rapid clearance with an estimated half-life $t_{1/2\alpha}$ = 6.5 ± 1.3 min from a one compartment modelization. Wash out from blood is even faster using the well-characterized $Au_{25}GSH_{18}$ (M~11 kDa)[31] in the same condition with $t_{1/2\alpha} = 1.2 \pm 0.2$ min. Those estimated half-life values are in the same order than previous *in vivo* studies using Au NCs stabilized by the tripeptide glutathione (GSH) reported by Zheng's team with $t_{1/2\alpha} = 5.4 \pm 1.2$ min with a NC size of 40 kDa[8] and by Chen *et al.* with $t_{1/2\alpha} = 0.7 \pm 0.1$ min.[6] This indicates first that reducing particle's size drastically shortens the blood circulation and suggests also that the zwitterionic ligand Zw coated on Au NCs leads to a longer blood circulation than GSH looking at the entire particle size. Non-invasive *in vivo* fluorescence imaging confirms the high renal clearance with the strong accumulation of Au:Zw 1:2

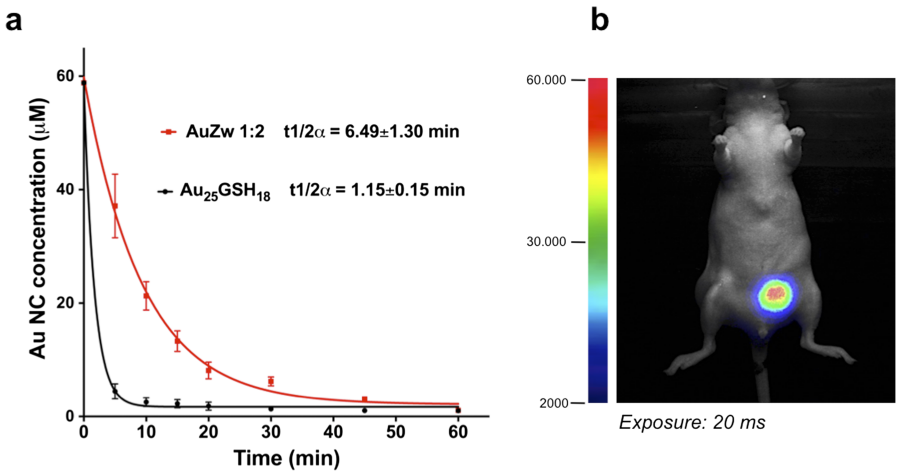

FIG. 5. (a) Blood pharmacokinetic of Au:Zw 1:2 and $Au_{25}GSH_{18}$ after intravenous injection (200 μL; 600 μM). Au NC concentration is determined from the fluorescence intensity values. (b) Non-invasive *in vivo* 2D fluorescence imaging 1 h after intravenous injection of Au:Zw 1:2 (600 μM, V = 200 μL) illustrating the strong elimination of Au NC by the bladder.

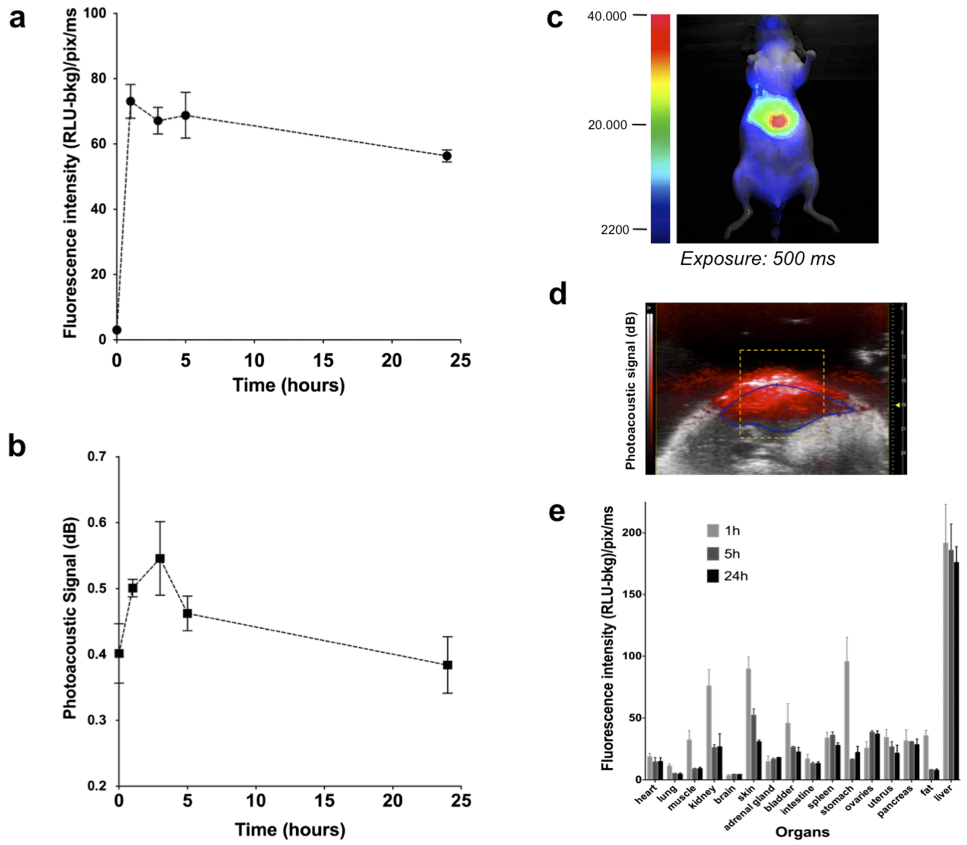

FIG. 6. Kinetic of Au:Zw 1:2 uptake in liver by (a) fluorescence and (b) photoacoustic imaging. (c) Non-invasive *in vivo* fluorescence (left) and (d) photoacoustic (right) imaging 3 h after Au:Zw 1:2 intravenous injection (200 μL; 600 μM). (e) Biodistribution analysis from *ex vivo* fluorescence imaging in different organs 1 h, 5 h, and 24 h after Au NC intravenous injection (200 μL; 600 μM).

in the bladder 1 h after intravenous injection (Figure 5(b)) in the same way that it was observed for others Au NCs.[6,7]

We evaluated the biodistribution of Au:Zw 1:2 in liver by using fluorescence imaging (Figures 6(a), 6(c), and 6(e)) and PAI (Figures 6(b), 6(d), and 6(e)) 1, 3, 5, and 24 h after intravenous injection. We found a good agreement between these two imaging techniques indicating an early accumulation of the Au NCs in the liver between 1 and 3 h followed by a slow elimination until 24 h. Mice were sacrificed at 1, 5, and 24 h and biodistribution analysis from *ex vivo* fluorescence imaging illustrated in Figure 6(e) shows the early elimination by kidney and bladder at 1 h post-injection which confirms the efficiency of kidney filtration for those Au NCs. The *ex vivo* data also indicate a weak fluorescence signal from all the other organs with the exception of the liver presenting an early uptake of Au NCs.

Herein, we demonstrate the ability to track gold nanoclusters (Au NCs) *in vivo* by two different imaging techniques based on 2D-NIR fluorescence and photoacoustic signal. Au NCs stabilized by a zwitterionic ligand could be synthesized by finely tuning the metal core size/ligand coverage in order to provide the best compromise fluorescence/photoacoustic signals. Those Au NCs displayed high renal clearance and both imaging techniques indicate an early Au NC uptake in liver. Therefore, the low toxicity and the detection of Au NCs by fluorescence imaging in the NIR region and by photoacoustic imaging make those contrast agents highly promising for future *in vivo* studies.

See supplementary material for the physico-chemical (TEM, XPS, ESI-MS) and optical (absorbance, fluorescence) properties of Au NCs.

Danjin Shen was financed by the Région Rhône Alpes (C'MIRA program). This work was realized at the small animal imaging technological platform OPTIMAL in the Institute of Advanced Biosciences (Grenoble, France). The Fluobeam800 fluorescence imaging device and the vevoLAZR photoacoustic imaging system were acquired thanks to France Life Imaging (FLI, French program "Investissement d'Avenir"; grant "Infrastructure d'avenir en Biologie Santé", ANR-11-INBS-0006). The K-Alpha+ instrument was financially supported by the Federal Ministry of Economics and Technology on the basis of a decision by the German Bundestag.

[1] M. Zhou, C. Zeng, Y. Chen, S. Zhao, M. Y. Sfeir, M. Zhu, and R. Jin, "Evolution from the plasmon to exciton state in ligand-protected atomically precise gold nanoparticles," Nat. Commun. **7**, 13240 (2016).
[2] J. Zheng, C. Zhou, M. Yu, and J. Liu, "Different sized luminescent gold nanoparticles," Nanoscale **4**, 4073–4083 (2012).
[3] R. Jin, "Quantum sized, thiolate-protected gold nanoclusters," Nanoscale **2**, 343–362 (2010).
[4] R. Jin, C. Zeng, M. Zhou, and Y. Chen, "Atomically precise colloidal metal nanoclusters and nanoparticles: Fundamentals and opportunities," Chem. Rev. **116**, 10346–10413 (2016).
[5] C. Zhou, M. Long, Y. Qin, X. Sun, and J. Zheng, "Luminescent gold nanoparticles with efficient renal clearance," Angew. Chem., Int. Ed. **50**, 3168–3172 (2011).
[6] F. Chen, S. Goel, R. Hernandez, S. A. Graves, S. Shi, R. J. Nickles, and W. Cai, "Dynamic positron emission tomography imaging of renal clearable gold nanoparticles," Small **12**, 2775–2782 (2016).
[7] J. Liu, M. Yu, C. Zhou, S. Yang, X. Ning, and J. Zheng, "Passive tumor targeting of renal-clearable luminescent gold nanoparticles: Long tumor retention and fast normal tissue clearance," J. Am. Chem. Soc. **135**, 4978–4981 (2013).
[8] J. Liu, M. Yu, X. Ning, C. Zhou, S. Yang, and J. Zheng, "PEGylation and zwitterionization: Pros and cons in the renal clearance and tumor targeting of near-IR-emitting gold nanoparticles," Angew. Chem., Int. Ed. **52**, 12572–12576 (2013).
[9] C. Zhang, C. Li, Y. Liu, J. Zhang, C. Bao, S. Liang, Q. Wang, Y. Yang, H. Fu, K. Wang, and D. Cui, "Gold nanoclusters-based nanoprobes for simultaneous fluorescence imaging and targeted photodynamic therapy with superior penetration and retention behavior in tumors," Adv. Funct. Mater. **25**, 1314–1325 (2015).
[10] X. D. Zhang, Z. Luo, J. Chen, S. Song, X. Yuan, X. Shen, H. Wang, Y. Sun, K. Gao, L. Zhang, S. Fan, D. T. Leong, M. Guo, and J. Xie, "Ultrasmall glutathione-protected gold nanoclusters as next generation radiotherapy sensitizers with high tumor uptake and high renal clearance," Sci. Rep. **5**, 8669 (2015).
[11] X. D. Zhang, Z. Luo, J. Chen, X. Shen, S. Song, Y. Sun, S. Fan, F. Fan, D. T. Leong, and J. Xie, "Ultrasmall $Au_{10\text{-}12}(SG)_{10\text{-}12}$ nanomolecules for high tumor specificity and cancer radiotherapy," Adv. Mater. **26**, 4565–4568 (2014).
[12] X. D. Zhang, J. Chen, Z. Luo, D. Wu, X. Shen, S. S. Song, Y. M. Sun, P. X. Liu, J. Zhao, S. Huo, S. Fan, F. Fan, X. J. Liang, and J. Xie, "Enhanced tumor accumulation of Sub-2 nm gold nanoclusters for cancer radiation therapy," Adv. Healthcare Mater. **3**, 133–141 (2014).
[13] A. Yahia-Ammar, D. Sierra, F. Mérola, N. Hildebrandt, and X. Le Guével, "Self-assembled gold nanoclusters for bright fluorescence imaging and enhanced drug delivery," ACS Nano **10**, 2591–2599 (2016).
[14] L. Shang, F. Stockmar, N. Azadfar, and G. U. Nienhaus, "Intracellular thermometry by using fluorescent gold nanoclusters," Angew. Chem., Int. Ed. **52**, 11154–11157 (2013).
[15] X. Le Guével, "Recent advances on the synthesis of metal quantum nanoclusters and their application for bioimaging," IEEE J. Sel. Top. Quantum Electron. **20**, 45–56 (2014).
[16] L. Zhang and E. Wang, "Metal nanoclusters: New fluorescent probes for sensors and bioimaging," Nano Today **9**, 132–157 (2014).
[17] L. Shang, N. Azadfar, F. Stockmar, W. Send, V. Trouillet, M. Bruns, D. Gerthsen, and G. U. Nienhaus, "One-pot synthesis of near-infrared fluorescent gold clusters for cellular fluorescence lifetime imaging," Small **7**, 2614–2620 (2011).
[18] J. V. Jokerst, M. Thangaraj, P. J. Kempen, R. Sinclair, and S. S. Gambhir, "Photoacoustic imaging of mesenchymal stem cells in living mice via silica-coated gold nanorods," ACS Nano **6**, 5920–5930 (2012).
[19] Y. S. Zhang, Y. Wang, L. Wang, Y. Wang, X. Cai, C. Zhang, L. V. Wang, and Y. Xia, "Labeling human mesenchymal stem cells with gold nanocages for *in vitro* and *in vivo* tracking by two-photon microscopy and photoacoustic microscopy," Theranostics **3**, 532–543 (2013).
[20] J. Xia, J. Yao, and L. V. Wang, "Photoacoustic tomography: Principles and advances," Prog. Electromagn. Res. **147**, 1–22 (2014).
[21] T. P. Matthews, K. Wang, L. V. Wang, M. A. Anastasio, "Synergistic image reconstruction for hybrid ultrasound and photoacoustic computed tomography," Proc. SPIE **9323**, 93233A (2015).
[22] L. V. Wang and S. Hu, "Photoacoustic tomography: *In vivo* imaging from organelles to organs," Science **335**, 1458–1462 (2012).
[23] Y. Yu, Z. Luo, D. M. Chevrier, D. T. Leong, P. Zhang, D. E. Jiang, and J. Xie, "Identification of a highly luminescent $Au_{22}(SG)_{18}$ nanocluster," J. Am. Chem. Soc. **136**, 1246–1249 (2014).
[24] Z. Wu, J. Chen, and R. Jin, "One-pot synthesis of $Au_{25}(SG)_{18}$ 2- and 4-nm gold nanoparticles and comparison of their size-dependent properties," Adv. Funct. Mater. **21**, 177–183 (2011).
[25] I. Russier-Antoine, F. Bertorelle, M. Vojkovic, D. Rayane, E. Salmon, C. Jonin, P. Dugourd, R. Antoine, and P. F. Brevet, "Non-linear optical properties of gold quantum clusters. The smaller the better," Nanoscale **6**, 13572–13578 (2014).
[26] Y. Negishi, K. Nobusada, and T. Tsukuda, "Glutathione-protected gold clusters revisited: Bridging the gap between gold(I)-thiolate complexes and thiolate-protected gold nanocrystals," J. Am. Chem. Soc. **127**, 5261–5270 (2005).
[27] T. A. Larson, P. P. Joshi, and K. Sokolov, "Preventing protein adsorption and macrophage uptake of gold nanoparticles via a hydrophobic shield," ACS Nano **6**, 9182–9190 (2012).
[28] X. Le Guével, O. Tagit, C. E. Rodríguez, V. Trouillet, M. Pernia Leal, and N. Hildebrandt, "Ligand effect on the size, valence state and red/near infrared photoluminescence of bidentate thiol gold nanoclusters," Nanoscale **6**, 8091–8099 (2014).

[29] X. Le Guével, M. Perez Perrino, T. D. Fernandez, F. Palomares, M. J. Torres, M. Blanca, J. Rojo, and C. Mayorga, "Multivalent glycosylation of fluorescent gold nanoclusters promotes increased human dendritic cell targeting via multiple endocytic pathways," ACS Appl. Mater. Interfaces **7**, 20945–20956 (2015).
[30] T. D. Fernandez, J. R. Pearson, M. Pernia Leal, M. J. Torres, M. Blanca, C. Mayorga, and X. Le Guével, "Intracellular accumulation and immunological properties of fluorescent gold nanoclusters in human dendritic cells," Biomaterials **43**, 1–12 (2015).
[31] E. S. Shibu, M. A. H. Muhammed, T. Tsukuda, and T. Pradeep, "Ligand exchange of $Au_{25}SG_{18}$ leading to functionalized gold clusters: Spectroscopy, kinetics, and luminescence," J. Phys. Chem. C **112**, 12168–12176 (2008).
[32] J. H. Scofield, "Hartree-Slater subshell photoionization cross-sections at 1254 and 1487 eV," J. Electron Spectrosc. Relat. Phenom. **8**, 129–137 (1976).
[33] J. Park, J. Nam, N. Won, H. Jin, S. Jung, S. Jung, S. H. Cho, and S. Kim, "Compact and stable quantum dots with positive, negative, or zwitterionic surface: Specific cell interactions and non-specific adsorptions by the surface charges," Adv. Funct. Mater. **21**, 1558–1566 (2011).
[34] F. Aldeek, M. A. H. Muhammed, G. Palui, N. Zhan, and H. Mattoussi, "Growth of highly fluorescent polyethylene glycol- and zwitterion- functionalized gold nanoclusters," ACS Nano **7**, 2509–2521 (2013).
[35] R. Hamouda, B. Bellina, F. Bertorelle, I. Compagnon, R. Antoine, M. Broyer, D. Rayane, and P. Dugourd, "Electron emission of gas-phase $[Au_{25}(SG)_{18}\text{-}6H]^{7-}$ gold cluster and its action spectroscopy," J. Phys. Chem. Lett. **1**, 3189–3194 (2010).
[36] Q. Xu, S. Kumar, S. Jin, H. Qian, M. Zhu, and R. Jin, "Chiral 38-gold-atom nanoclusters: Synthesis and chiroptical properties," Small **10**, 1008–1014 (2014).
[37] Y. Yu, Z. Luo, J. Y. Lee, and J. Xie, "Observation of cluster size growth in CO-directed synthesis of $Au_{25}(SR)_{18}$ nanoclusters," ACS Nano **6**, 7920–7927 (2012).
[38] L. A. Angel, L. T. Majors, A. C. Dharmaratne, and A. Dass, "Ion mobility mass spectrometry of $Au_{25}(SCH_2CH_2Ph)_{18}$ nanoclusters," ACS Nano **4**, 4691–4700 (2010).
[39] R. Hamouda, F. Bertorelle, D. Rayane, R. Antoine, M. Broyer, and P. Dugourd, "Glutathione capped gold $Au_N(SG)_M$ clusters studied by isotope-resolved mass spectrometry," Int. J. Mass Spectrom. **335**, 1–6 (2013).
[40] Y. Lu and W. Chen, "Application of mass spectrometry in the synthesis and characterization of metal nanoclusters," Anal. Chem. **87**, 10659–10667 (2015).
[41] C. Truillet, F. Lux, O. Tillement, P. Dugourd, and R. Antoine, "Coupling of HPLC with electrospray ionization mass spectrometry for studying the aging of ultrasmall multifunctional gadolinium-based silica nanoparticles," Anal. Chem. **85**, 10440–10447 (2013).
[42] J. J. Hagen and C. A. Monnig, "Method for estimating molecular mass from electrospray spectra," Anal. Chem. **66**, 1877–1883 (1994).
[43] S. Link and M. A. El-Sayed, "Shape and size dependence of radiative, non-radiative and photothermal properties of gold nanocrystals," Int. Rev. Phys. Chem. **19**, 409–453 (2000).
[44] I. Atallah, C. Milet, M. Henry, V. Josserand, E. Reyt, J. L. Coll, A. Hurbin, and C. A. Righini, "Near-infrared fluorescence imaging-guided surgery improves recurrence-free survival rate in novel orthotopic animal model of head and neck squamous cell carcinoma," Head Neck **38**, E246–E255 (2016).
[45] V. Josserand, M. Kéramidas, J. Lavaud, C. Righini, J. Vollaire, E. Bellard, M. P. Rols, J. Teissié, J. L. Coll, and M. Golzio, "Electrochemotherapy guided by intraoperative fluorescence imaging for the treatment of inoperable peritoneal micro-metastases," J. Controlled Release **233**, 81–87 (2016).
[46] K. Pyo, V. D. Thanthirige, K. Kwak, P. Pandurangan, G. Ramakrishna, and D. Lee, "Ultrabright luminescence from gold nanoclusters: Rigidifying the Au(I)-thiolate shell," J. Am. Chem. Soc. **137**, 8244–8250 (2015).
[47] L. Yang, L. Shang, and G. U. Nienhaus, "Mechanistic aspects of fluorescent gold nanocluster internalization by live HeLa cells," Nanoscale **5**, 1537–1543 (2013).